The Astrophysical Journal, 955:146 (12pp), 2023 October 1 https://doi.org/10.3847/1538-4357/acdeeb

Evolution of Elemental Abundances in Hot Active Region Cores from Chandrayaan-2 XSM Observations

Biswajit Mondal[1,2], Santosh V. Vadawale[1], Giulio Del Zanna[3], N. P. S. Mithun[1], Aveek Sarkar[1], Helen E. Mason[3], P. Janardhan[1], and Anil Bhardwaj[1]
[1] Physical Research Laboratory, Navrangpura, Ahmedabad, Gujarat-380 009, India; biswajit70mondal94@gmail.com,
[2] Indian Institute of Technology Gandhinagar, Palaj, Gandhinagar, Gujarat-382 355, India
[3] DAMTP, Centre for Mathematical Sciences,University of Cambridge, Wilberforce Road, Cambridge, CB3 0WA, UK
Received 2023 January 9; revised 2023 May 22; accepted 2023 June 6; published 2023 September 27

Abstract

The first ionization potential (FIP) bias, whereby elemental abundances for low-FIP elements in different coronal structures vary from their photospheric values and may also vary with time, has been widely studied. In order to study the temporal variation and understand the physical mechanisms giving rise to the FIP bias, we have investigated the hot cores of three active regions (ARs) using disk-integrated soft X-ray spectroscopic observations with the Solar X-ray Monitor on board Chandrayaan-2. Observations for periods when only one AR was present on the solar disk were used to ensure that the AR was the principal contributor to the total X-ray intensity. The average values of temperature and emission measure were ∼3 MK and 3×10^{46} cm^{-3}, respectively. Regardless of the AR's age or activity, the elemental abundances for the low-FIP elements Al, Mg, and Si with respect to the soft X-ray continuum were consistently higher than their photospheric values. The average FIP bias for Mg and Si was 2–2.5, whereas the FIP bias for the mid-FIP element, S, was almost unity. However, the FIP bias for the lowest-FIP element, Al, was observed to be a factor of 2 higher than Si, which, if real, suggests a dependence of the FIP bias of low-FIP elements on their FIP value. Another major result from our analysis is that the FIP bias of these elements is established within ∼10 hr of emergence of the AR and remains almost constant throughout its lifetime.

Unified Astronomy Thesaurus concepts: Active solar corona (1988); Solar abundances (1474); Solar active regions (1974); Solar x-ray emission (1536)

1. Introduction

The earlier study of the Sun as a star by Pottasch (1963) revealed that solar coronal abundances are different from those of the photosphere. The differences are correlated to the first ionization potential (FIP) of the element, in the sense that the abundance ratio of a low-FIP (less than 10 eV) element versus that of a high-FIP element is higher in the corona. A measure of the difference is the so-called FIP bias, i.e., the ratio between the coronal and photospheric abundance of an element.

The FIP bias is generally estimated by measuring the relative abundances between elements, rather than to hydrogen. This is due to the fact that abundance measurements with respect to hydrogen in the low corona are nontrivial. Hence, whether it is the low-FIP elements that have an increased abundance or the high-FIP elements that have a reduced one (compared to their photospheric values) is unclear.

Further, it has become clear that different solar structures have different FIP biases. There are also indications that the FIP bias depends on the temperature of the plasma. For a long time, it has been widely accepted that coronal abundances in active regions (ARs) increase with time. We refer the reader to the recent reviews by Laming (2015) and Del Zanna & Mason (2018) for more details.

Knowledge of the elemental abundances in different atmospheric layers of the Sun is a topic of great interest to the solar physics community, mainly for the following two reasons. The first is that they provide, in principle, a way to link the solar source regions to the various components of the solar wind (SW). In fact, elemental abundance variations are also clearly observed in situ. The slow-speed SW has a high FIP bias similar to that measured in AR core loops, 3 MK, whereas the high-speed wind has a near unit FIP bias, similar to that of coronal holes (see, e.g., Gloeckler & Geiss 1989; Feldman et al. 1998; Bochsler 2007; Brooks & Warren 2011; Brooks et al. 2015).

The second reason is that studying abundance variations contributes to a better understanding of the physical processes at play in the solar corona. In fact, we know that the FIP bias is closely related to the magnetic field activity of the Sun (see, e.g., Feldman & Widing 2002; Brooks et al. 2017; Baker et al. 2018). The ponderomotive force model (Laming 2004, 2009, 2012, 2017) is now widely accepted as being able to reproduce the main characteristics of the FIP effect, as measured in situ and remotely. According to this model, the separation of ions from neutral atoms within closed loops in an upward direction is caused by the reflection of downward-propagating Alfvén waves at chromospheric heights causing an enhancement of the low-FIP elements in the corona. Since coronal waves can be produced by mechanisms that heat the solar corona, it is thought that the mechanism underlying the FIP effect is inextricably linked to processes that heat the solar corona. Hence, measuring the FIP bias is an important diagnostic for coronal plasma characteristics (Laming 2015; Dahlburg et al. 2016).

In this paper, we focus on the elemental abundances of hot, quiescent AR core emission at 3 MK by providing line-to-continuum measurements of the Sun in the soft X-ray energy band using data from the Solar X-ray Monitor (XSM;

Vadawale et al. 2014; Shanmugam et al. 2020). It may be noted here that the XSM is the only spectrometer to have observed the Sun in the 1–15 keV range during the minimum of solar cycle 24 with an energy resolution better than 180 eV at 5.9 keV. This resolution is sufficient to measure the abundances of several elements.

The XSM energy band is sensitive to temperatures above 2 MK. When the Sun was at minimum activity levels, without any ARs, the XSM observed a steady signal originating from X-ray bright points (XBPs) with a peak emission around 2 MK (Vadawale et al. 2021b). When a single nonflaring AR is present, the signal is dominated by the AR's near-isothermal ∼3 MK emission (see, e.g., Del Zanna 2013). This provides an excellent opportunity to measure the FIP bias or abundance of the hot AR core with respect to the continuum. However, the soft X-ray continuum for 3 MK AR plasma is dominated by free–bound emission, which depends on abundant elements (e.g., O, Ne, etc.), as detailed in Appendix C. Therefore, the measured abundances are actually relative abundances.

In the literature, few abundance measurements are known to be associated specifically with the 3 MK emission from quiescent AR cores. These are summarized in Del Zanna & Mason (2018). The X-ray spectra in the 10–20 Å range have provided the relative abundances of the low-FIP elements, Fe, Mg with respect to high-FIP elements, O, and Ne. Saba & Strong (1993) reported a significant variability of the FIP bias using SMM/FCS observations of several ARs. On the other hand, a reanalysis of several quiescent AR cores with improved atomic data and using a differential emission measure (DEM) technique by Del Zanna & Mason (2014) indicated the same FIP bias, around 3, for all of the ARs studied, irrespective of their age and size.

Since 2006, extreme-ultraviolet (EUV) spectra from the Hinode EIS instrument have provided an opportunity to measure the relative FIP bias between low-FIP elements (e.g., Fe and Si) and the high-FIP element Ar, as well as the mid-FIP element S. The latter actually shows the same abundance variations as the high-FIP elements. An example case was discussed by Del Zanna (2013), showing that the FIP bias in the EUV of 3 MK plasma was the same as in the X-rays. Considering the size of the emitting plasma and its emission measure (EM), Del Zanna (2013) concluded that it should be the low-FIP elements that are overabundant by about a factor of 3.

Del Zanna et al. (2022) carried out a multiwavelength study of an AR as it crossed the solar disk that was observed by XSM, as well as by SDO/AIA, Hinode/EIS, and Hinode/XRT. The relative FIP bias obtained from Hinode/EIS observations confirmed the Del Zanna (2013) results and showed no variation with the disk passage. The analysis of simultaneous XSM spectra on two nonflaring periods of different days also indicated no significant variability and provided an FIP bias for Si of 2.4, i.e., close to the value suggested by Del Zanna (2013) and very close to the prediction of Laming's model.

In the present study, we extend the previous XSM analysis to all quiescent periods of that same AR and investigate two other ARs during their disk crossings. One AR in particular is of interest, as it emerged on-disk and hence offers the opportunity to study the elemental abundances during the early phase of the evolution of an AR.

The rest of the paper is organized as follows. Section 2 provides a short overview of previous abundance measurements in ARs. Section 3 describes the observations and data analysis. Section 4 provides a detailed spectral analysis. After obtaining the results, they are discussed in Section 5. Section 6 provides a brief summary of the paper.

2. Historical Overview

Spatially resolved measurements of the relative FIP bias have been carried out by several authors (see, e.g., Widing & Feldman 1993, 2001; Sheeley 1995, 1996; Widing 1997) using Skylab spectroheliograms with Mg and Ne transition region lines. These are formed well below 1 MK, in the legs of "cool" (1 MK) AR loops. They found photospheric composition (FIP bias = 1) for newly emerged closed loops but increasing FIP bias reaching a value of 3–4 within a timescale of 1–2 days (Widing & Feldman 2001) and much higher values, up to about 10, within a few more days. Differing FIP biases were also obtained by Young & Mason (1997) and Dwivedi et al. (1999) using Mg and Ne line ratios observed by the CDS and SUMER spectrometers on board the Solar and Heliospheric Observatory (SOHO).

The large values for the FIP bias (around 10) are hard to reconcile with in situ measurements, where the FIP bias is at most 3, as well as with theory. However, Del Zanna (2003) pointed out that as the cool AR loops are almost isothermal in their cross sections, the assumption that a smooth EM distribution was present in the plasma, used to interpret the Skylab data, was not justified. Del Zanna (2003) took the intensities measured by Widing & Feldman (1993) and, using an EM loci approach, showed that an FIP bias of 3.7 was consistent with the data, much lower than the value of 14 reported by Widing & Feldman. Del Zanna (2003) also analyzed the legs of several cool loops observed by SOHO/CDS and found photospheric abundances, although a similar analysis for other loops by Del Zanna & Mason (2003) found an FIP bias of 4.

In summary, the legs of cool AR loops do show a range of FIP bias values between 1 and 4 and perhaps occasionally larger. However, the very high FIP biases found from Skylab data were largely overestimated.

As shown by Del Zanna & Mason (2003), AR cores are composed not only of cool 1 MK loops and unresolved, almost isothermal 3 MK loops but also unresolved emission in the 1–3 MK range. The plasma at different temperatures is generally not cospatial.

There is evidence from Hinode/EIS observations of, for example, the Si X AND S X lines that this ≃2 MK emission has a lower relative FIP bias of around 2 (see, e.g., Del Zanna 2012). Further studies using the same lines (e.g., Baker et al. 2013, 2015; Ko et al. 2016; Doschek & Warren 2019; Mihailescu et al. 2022; Testa et al. 2022) have shown some variation (around a value of 2) of the relative FIP bias within each AR but little variability in time except during the decay phase, when the AR effectively disappears and the relative abundances become photospheric.

In summary, AR structures formed at temperatures below 2 MK show a range of relative FIP biases and some temporal variability. The few observations of the hotter, 3 MK, AR cores have shown, in contrast, a remarkable consistency, with relative FIP biases of around 3.

Finally, to interpret the observations of the Sun as a star, one needs to take into account the above (and other) issues. As shown by Del Zanna (2019), when the Sun's activity is at a minimum with no AR present on the solar disk, the corona around 1 MK shows near-photospheric abundances, whereas in the presence of ARs, the FIP bias for the 1 MK emission stays the same, but the hotter emission shows a higher relative FIP bias. When ARs flare, the high-temperature plasma shows nearly photospheric composition around the peak X-ray emission (see, e.g., Mondal et al. 2021).

3. Observations and Data Analysis

Observations of the Sun were carried out with XSM during the minimum of solar cycle 24, when no ARs were present, in 2019–2020. The results are given in Vadawale et al. (2021b). They reported intermediate abundances of low-FIP elements (Mg, Al, and Si) of 2 MK plasma, primarily originating from XBPs (Mondal et al. 2023). Frequent microflaring activity was observed and found to be occurring everywhere on the solar disk, even when no ARs were present (Vadawale et al. 2021a). During the minimum of solar cycle 24, XSM observed the disk passage of a few individual, isolated ARs in the absence of any other major activity. When ARs were present on-disk, XSM recorded hundreds of small flares of different classes. Elemental abundance variations during these small flares were found, for the first time, to initially drop toward photospheric values, then rapidly return to coronal values, as described by Mondal et al. (2021), Mithun et al. (2022), and Nama et al. (2023). In this paper, we analyze the temporal evolution of ARs outside of flaring activity, and for this, we have chosen to study three isolated ARs: AR 12749, AR 12758, and AR 12759.

The XSM data contain spectra at 1 s cadence in a raw (level 1) daily file. Since the visibility of the Sun varies within the XSM field of view (FOV), with the Sun sometimes being outside the FOV or occulted by the Moon, the data include both solar and nonsolar spectra. The XSM Data Analysis Software (XSMDAS: Mithun et al. 2021) has been used to generate the level 2 science data product using the appropriate good time intervals (GTIs) and other necessary instrumental parameters. The available default level 2 data contain the effective area-corrected light curves for every second and spectra for every minute. The XSMDAS also provides the functionality to generate the light curves and spectra for a given cadence and energy range, which we have used in the present analysis.

Using XSMDAS, we have generated 2 minute averaged XSM light curves in the energy range of 1–15 keV during the disk passage of AR 12749, AR 12758, and AR 12759, as shown in the three panels of Figure 1. During the evolution of these three ARs, representative full-disk X-ray images taken by the XRT Be thin filter are shown in the top row of each panel. The AR 12749 (Figure 1(a)) appeared from the east limb on 2019 September 29. While crossing the solar disk, it became fainter toward the west limb and went behind the limb on October 14. The AR 12758 (Figure 1(b)) appears to form on the disk on 2020 March 6 and has fully emerged after March 8. It decays while crossing the solar disk and finally goes behind the west limb on March 18. The AR 12759 appeared from the east limb on 2020 March 29 and transited the solar disk until 2020 April 14 before disappearing behind the west limb.

The full-disk XRT images show that during the passage of these three ARs, no other major activity was present on the solar disk. Thus, we conclude that these three ARs were primarily responsible, during their disk passage, for the enhanced X-ray emission observed by the XSM. These ARs produced many small B/A-class flares, seen as multiple spikes in the XSM light curves. Detailed studies of these small flares were reported by Mondal et al. (2021) and Nama et al. (2023).

In the present study, we have selected only the quiescent periods from the observed light curves by excluding the periods when the small flares occurred using a semiautomated graphical algorithm. For example, Figure 2 shows the representative selection (orange shaded regions) for 1 day of AR 12749 (panel (a)), AR 12758 (panel (b)), and AR 12759 (panel (c)). These identified time intervals were used as user-defined GTIs to generate the spectra for quiescent ARs on a daily basis in order to carry out the detailed spectral analysis as discussed in Section 4.

4. Spectral Analysis

The broadband soft X-ray spectra of the solar corona consist of a continuum, as well as the emission lines of the different elements. Modeling the soft X-ray spectrum provides the measurements of the temperature, EM, and elemental abundances (with respect to continuum emission) of the emitting plasma (Del Zanna & Mason 2018). We use the `chisoth` model (see the Appendix in Mondal et al. 2021) for the spectral fitting. The `chisoth` is a local model of the X-ray spectral fitting package (XSPEC; Arnaud et al. 1999), and it estimates the theoretical spectrum using the CHIANTI atomic database. It takes the temperature, EM (which is related to the density of the plasma), and elemental abundances of the elements from $Z = 2$ to 30 as free variables for the spectral fitting.

After generating the spectra for the quiescent periods, we fitted them with an isothermal emission model. For the spectral fitting, we ignored the spectra below 1.3 keV, where the XSM response is not well known (Mithun et al. 2020), and above the energy where the spectrum is dominated by the nonsolar background spectrum. During the spectral fitting, the temperature, EM, and abundances of Mg, Al, and Si (whose emission lines are prominent in the XSM spectrum) were kept as variable parameters. The 1σ uncertainty of each free parameter was also estimated using the standard procedure in XSPEC.

Although the S line complex is visible in the spectra, including it in the spectral fits as a free parameter causes a large uncertainty in the measurement of the S abundance because of its poor statistics. Hence, in the `chisoth` model, we fixed the S abundances along with the abundances of other elements (whose emission lines are not visible in the observed spectra) with the photospheric abundances of Asplund et al. (2009). However, we found that the measurement of the S abundance is possible for the statistically improved summed spectra of the entire AR period.

It should be noted that the measured abundances are with respect to the continuum emission, which has contributions from free–free, two-photon, and free–bound processes (see Appendix C). For AR temperatures of around 3 MK, the main contribution to the continuum is free–bound, mostly (nearly 80%) by O and Ne (see Appendix C). As the observed spectra do not have any emission lines of O and Ne, their abundances cannot be measured from the fitting. Therefore, in our abundance measurements, we have to assume a reasonable value of the O and Ne abundances for an AR. In measurements and models of the FIP effect, it is common to use oxygen as a reference point and measure other abundances relative to

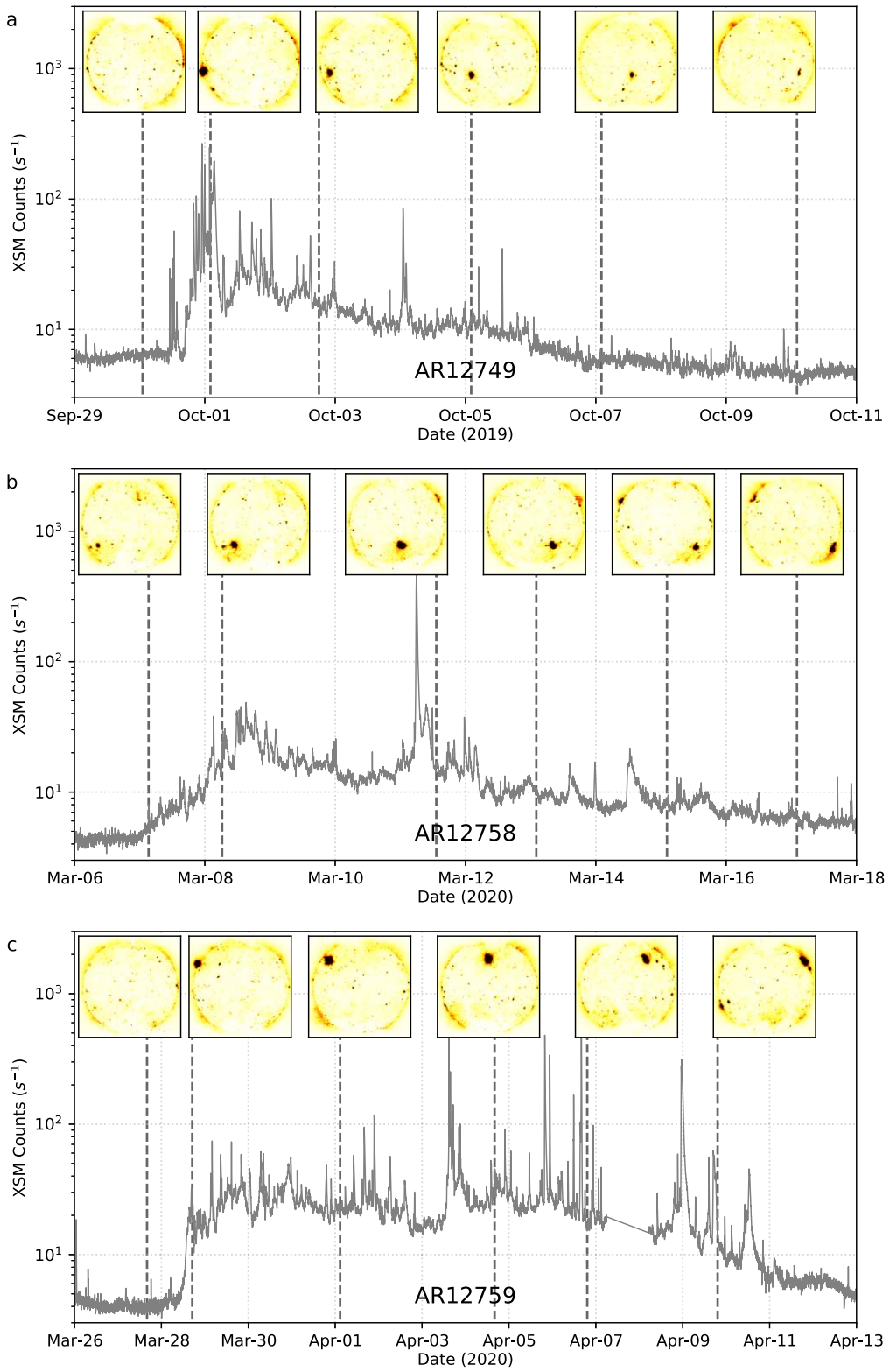

Figure 1. The XSM 1–15 keV light curves during the disk passage of AR 12749 (panel (a)), AR 12758 (panel (b)), and AR 12759 (panel (c)). The top row of each panel shows representative full-disk X-ray images (negative intensities) taken with the XRT Be thin filter during the evolution of the ARs. The vertical dashed lines represent the timing of the XRT images.

oxygen. As the FIP for oxygen is close to that of hydrogen, it is often assumed that it is not fractionated and hence has a photospheric abundance.

A direct measurement of O/H abundance is challenging. However, we do have direct in situ measurements of O/H abundance in the SW. The measurements of the O/H abundance in the SW show a scatter centered around 8.8 dex (see Bame et al. 1975; Von Steiger et al. 2010), which is close to the photospheric value (∼8.7 dex) recommended by Asplund et al. (2009, 2021). As most high-FIP elements, such

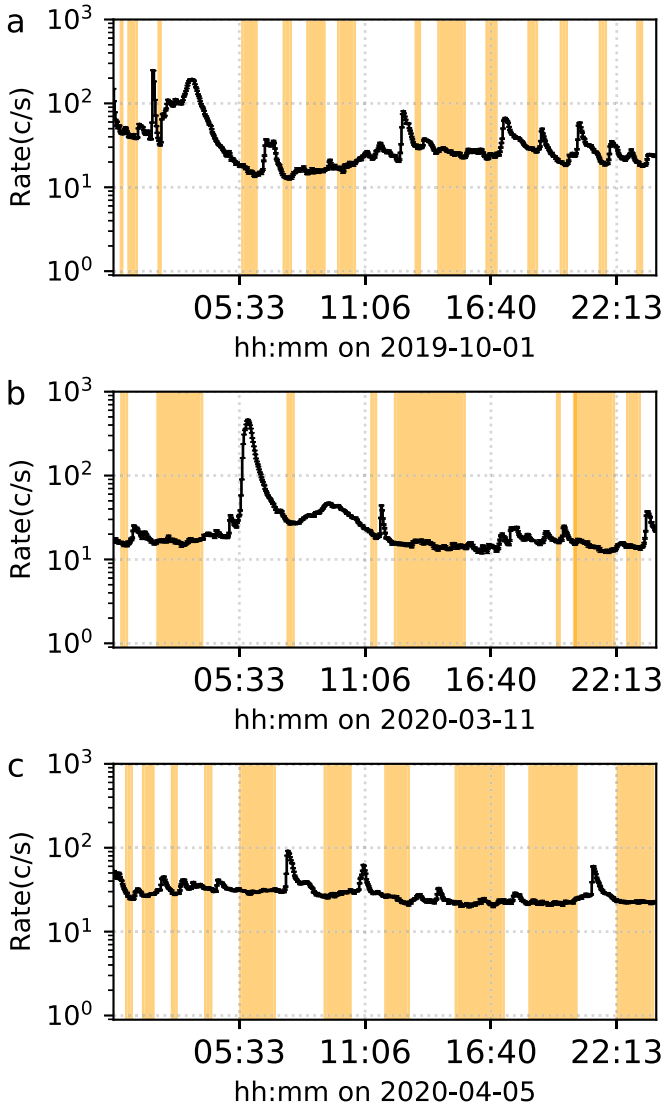

Figure 2. Selection of the quiescent AR periods (orange shaded regions) from the XSM light curves for 1 representative day of AR 12749 (panel (a)), AR 12758 (panel (b)), and AR 12759 (panel (c)).

as Ne, show similar abundance variations as O, it is reasonable to assume that the coronal abundance of Ne (C, N) will also have a value close to photospheric. Therefore, we have fixed the abundances of Ne, C, and N to the values recommended by Asplund et al. (2009). It is noted that fixing the abundance of these elements, except O, to their coronal values reported in the literature (e.g., Feldman 1992; Fludra & Schmelz 1999) does not vary the measured abundance of Mg, Al, Si, and S significantly. They remain within the error bars.

Figure 3 shows the representative XSM spectra for the three ARs fitted in different colors with an isothermal model. The points with error bars represent the observed spectra, whereas the solid curves represent the best-fit modeled spectra. The gray error bars represent the nonsolar background spectrum, which is subtracted from the observed spectra during the spectral analysis. The bottom panel shows the residuals between the observed and model spectra. We have fitted all of the spectra in a similar way and found that all of them are well described by an isothermal model.

The X-rays observed by XSM originated from both the AR and the background quiet-Sun regions (outside the AR). To determine

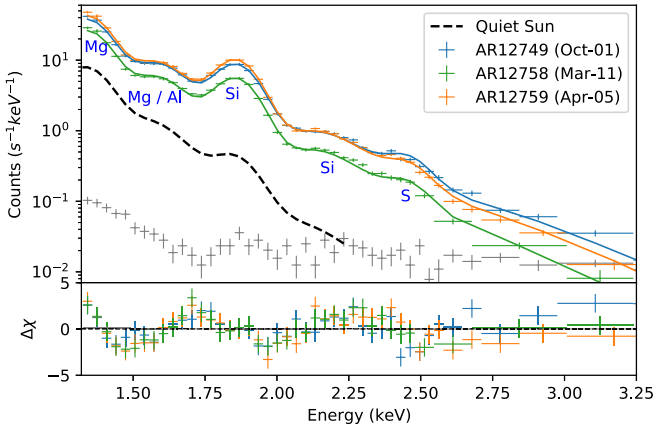

Figure 3. Soft X-ray spectra measured by XSM for 3 representative days of the AR period are shown. Solid lines represent the best-fit isothermal model, and the residuals are shown in the bottom panel. Gray points correspond to the nonsolar background spectrum. The black dashed curve in the above panel represents the average quiet-Sun spectrum.

how much emission is due to the background quiet-Sun regions, we estimate the average quiet-Sun spectrum using an average quiet-Sun temperature, EM, and abundances as reported by Vadawale et al. (2021b). The average quiet-Sun spectrum is shown by the black dashed curve in Figure 3. The quiet-Sun spectrum is found to be almost an order of magnitude lower than the spectra of the active period when the ARs were very bright on the solar disk. We thus conclude that the X-ray emission of the active periods is primarily dominated by the AR emission.

Separating the AR emission from the background quiet-Sun emission would be possible by subtracting the quiet-Sun spectra from the AR spectra. But, as the effective area of the XSM varies with time, this is not recommended. It is possible to model the AR spectra using a two-temperature (2T) component model rather than subtracting the quiet-Sun spectra. This is what we have chosen to do. One temperature corresponds to the background solar emission originating from the regions outside the AR, and the second temperature corresponds to the AR plasma. We have modeled a few AR spectra with a 2T model. During the 2T spectral fitting, the parameters of the background solar emission were kept fixed to the average quiet-Sun values reported by Vadawale et al. (2021b). For the AR component, the temperature and EM, along with the abundances of Mg, Al, and Si, were kept as variable parameters. We found that the 2T model can describe the XSM spectra for the active periods with similar best-fit parameters as those obtained by the isothermal model. This verifies that the AR emission dominates the spectra of the AR periods. Thus, in this study, we show the results of the isothermal analysis in Figures 5 and 6. This is discussed in Section 5.

It is interesting to study how the plasma parameters vary during the emerging phase of AR 12758, i.e., from 2020 March 7 to 2020 March 9. Figure 4 shows the evolution of the photospheric magnetograms (top row) and X-ray emission (bottom row) as observed by SDO/HMI and the Be thin filter of Hinode/XRT, respectively. These images were created by derotating the synoptic data of HMI[4] and XRT[5] to a common date (2020 March 8) using the standard procedure of SolarSoftWare (Freeland & Handy 1998). We also determined the total unsigned photospheric magnetic flux for a threshold

[4] http://jsoc.stanford.edu/data/hmi/synoptic/
[5] http://solar.physics.montana.edu/HINODE/XRT/SCIA/

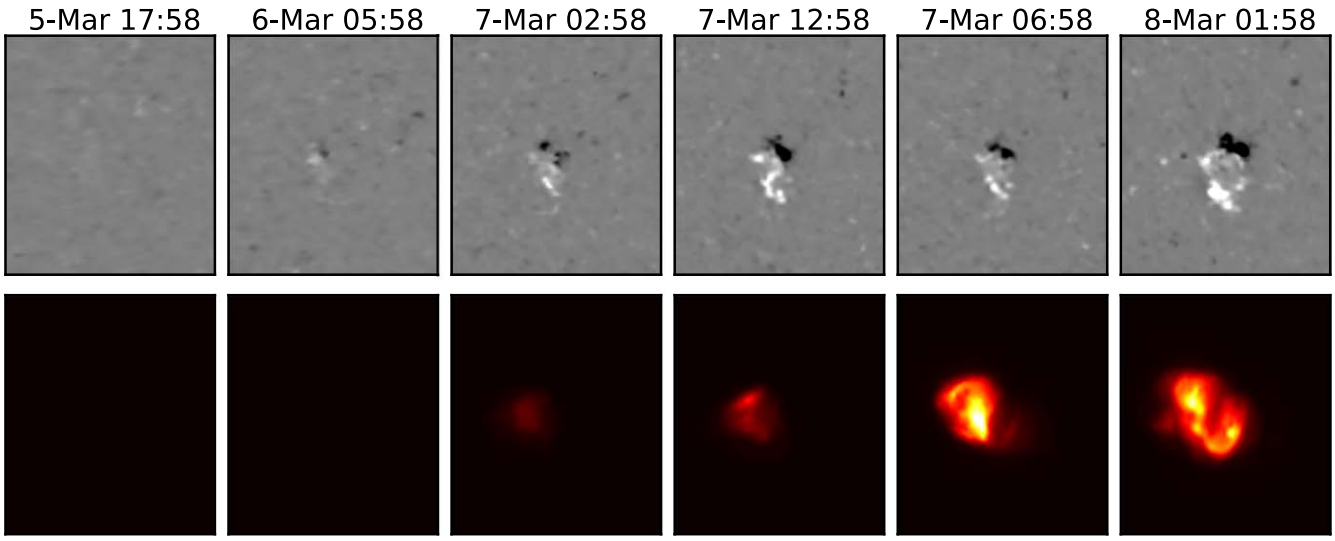

Figure 4. Evolution of AR 12758 during its emergence phase on the solar disk. The top row shows the evolution of the photospheric magnetograms as observed by HMI, and the bottom row shows the evolution of the X-ray emission as observed by the XRT Be thin filter.

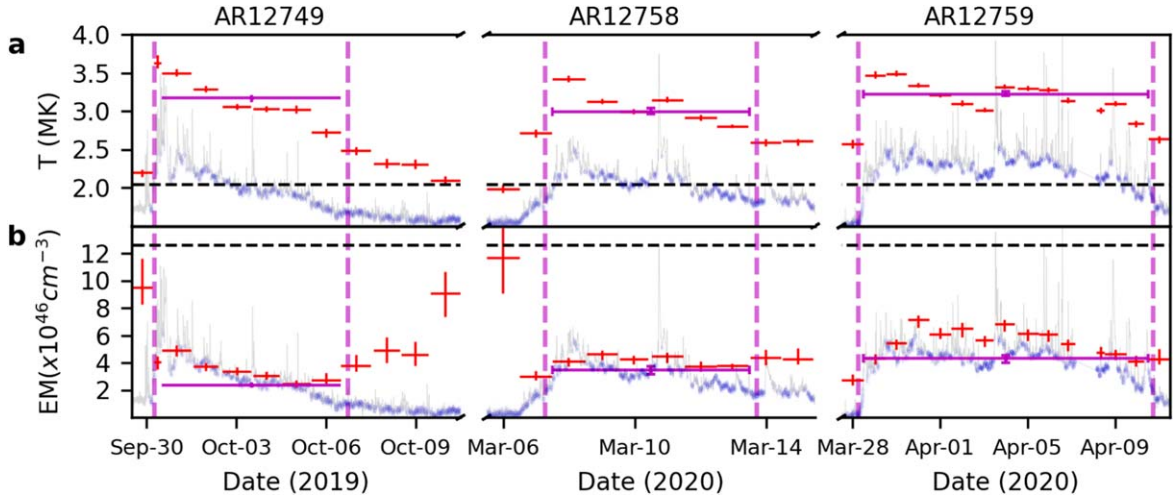

Figure 5. Evolution of the temperature (red points in panel (a)) and EM (red points in panel (b)) during the evolution of AR 12749, AR 12758, and AR 12759. When the ARs are very bright, as bounded by the vertical dashed lines, the magenta bars represent the average values of the temperature and EM. The black horizontal dashed lines represent the average temperature and EM for the quiet Sun in the absence of any AR reported by Vadawale et al. (2021b). The XSM light curves of the ARs are shown in gray, and the light curves for the quiescent regions are shown in blue.

magnetic field above |10| G, within the FOV shown in Figure 4. During this emerging flux period, we carried out a time-resolved spectroscopic study using the XSM observations with finer time bins of less than a day. However, during this period, as the emission from the AR was not very bright, the emission from the AR and the rest of the Sun could have been mixed together. Thus, to derive the evolution of the plasma parameters during this period, we modeled the observed XSM spectra with a 2T model, where one component represents the emission from the AR and the other represents the emission from the rest of the Sun, as discussed in the previous paragraph. The results are shown in Figure 7 and discussed in Section 5.

5. Results and Discussion

In this study, we have performed the X-ray spectral analysis for the evolution of three ARs as observed by XSM. The AR spectra (Figure 3) show a clear signature of the thermal X-ray emission from the line complexes of Mg, Al, Si, and S, along with the continuum emission up to ∼3.0 keV. The red points in Figure 5 show the evolution of the temperature and EM throughout the evolution of the three ARs. Figure 6 shows the evolution of abundances of Mg (panel (a)), Al (panel (b)), and Si (panel (c)). The error bars associated with all of the parameters along the y-axis represent the 1σ uncertainties. We also derived the average S abundance along with the other elements from the summed spectrum for the duration when the ARs were very bright on the solar disk (bounded by the vertical dashed lines in Figures 5 and 6). This provides the average parameters associated with each AR, as shown by magenta bars and given in Table 1. The primary findings of the paper are discussed below.

5.1. Temperature and Emission Measure

Temperatures (T) and EMs are close to the quiet-Sun levels (black dashed lines in Figure 5) when the ARs are absent from the solar disk or only partially present, e.g., 2019 September 30

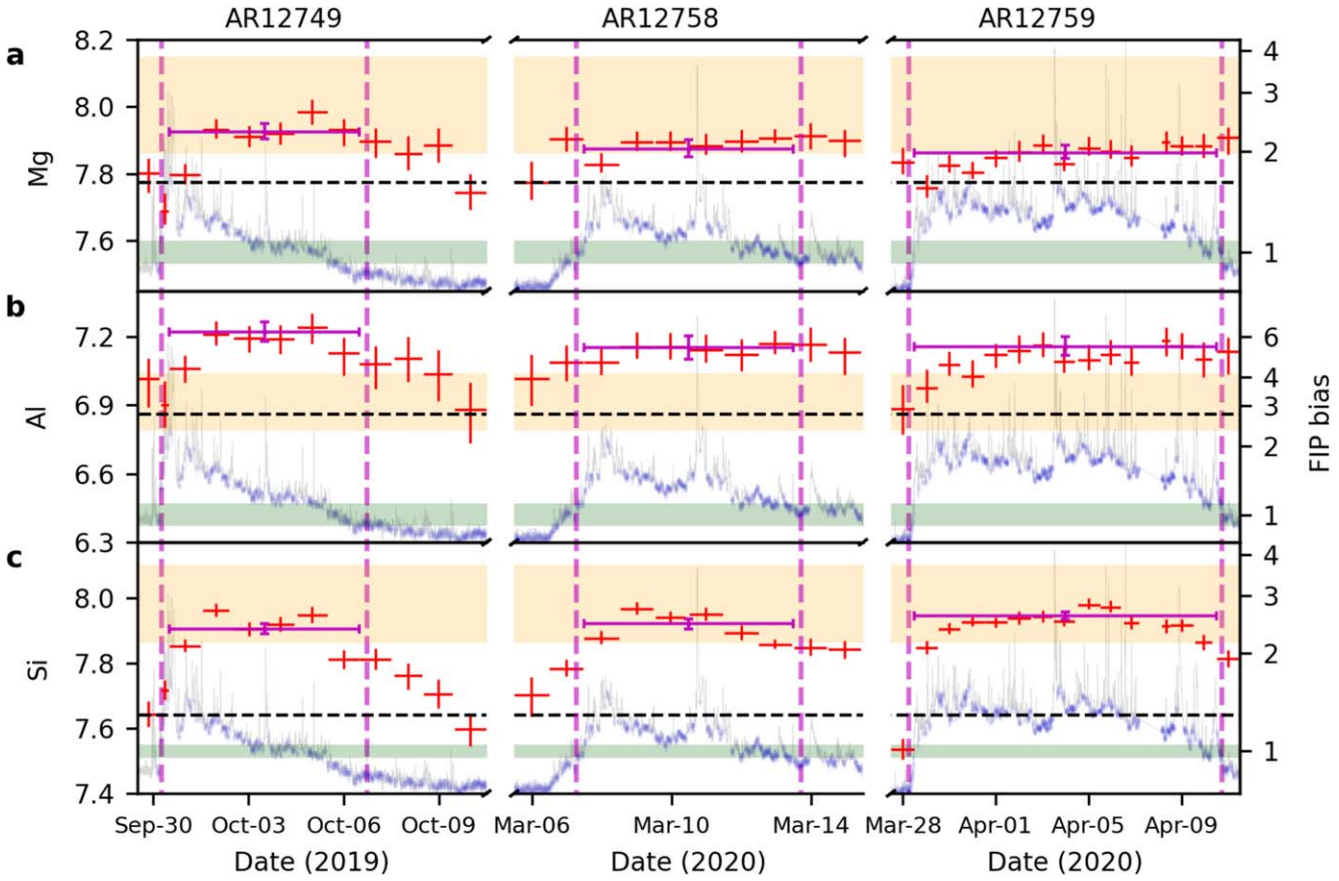

Figure 6. Panels (a)–(c) (red error bars) show the evolution of abundance in the logarithmic scale with $A(\mathrm{H}) = 12$ for Mg, Al, and Si during the evolution of AR 12749, AR 12758, and AR 12759. These abundances are measured with respect to the soft X-ray continuum, which is mostly determined by the choice of oxygen abundance, which was considered to be 8.8 dex. The magenta bars represent the average abundances when the ARs are very bright, as bounded by the vertical dashed lines. The *y*-error bars represent the 1σ uncertainty for each parameter, and the *x*-error bars represent the duration over which a given spectrum is integrated. The black horizontal dashed lines represent the average abundances for the quiet Sun in the absence of any AR reported by Vadawale et al. (2021b). The XSM light curves for each AR are shown in gray in the background, and the blue XSM light curves represent the time duration excluding the flaring activities. The range of coronal and photospheric abundances from various authors compiled in the CHIANTI database is shown as orange and green bands. The right *y*-axis shows the FIP bias values for the respective elements with respect to the average photospheric abundances.

Table 1
Best-fit Parameters for the Average Spectrum of Each AR

AR	T (MK)	EM (10^{46} cm^{-3})	Mg	Al	Si	S
12749	$3.22^{+0.04}_{-0.04}$	$2.78^{+0.21}_{-0.20}$	$7.93^{+0.02}_{-0.02}$	$7.22^{+0.04}_{-0.04}$	$7.90^{+0.02}_{-0.02}$	$7.07^{+0.04}_{-0.05}$
12759	$3.24^{+0.04}_{-0.02}$	$5.41^{+0.23}_{-0.35}$	$7.86^{+0.02}_{-0.02}$	$7.15^{+0.05}_{-0.04}$	$7.94^{+0.01}_{-0.01}$	$7.13^{+0.02}_{-0.03}$
12758	$3.04^{+0.05}_{-0.03}$	$4.14^{+0.28}_{-0.36}$	$7.87^{+0.03}_{-0.02}$	$7.15^{+0.05}_{-0.05}$	$7.92^{+0.02}_{-0.02}$	$7.18^{+0.04}_{-0.06}$

and 2020 March 6. Once the ARs appear, the temperature rises to more than ∼3 MK from the ∼2 MK of the quiet Sun. As the ∼3 MK emission is predominantly derived from a smaller volume of AR plasma, the presence of the AR reduces the EM from the quiet-Sun values. The average temperatures for all of the ARs are determined to be ∼3 MK (magenta error bars in Figure 5(a)), which is close to the "basal" temperature of the AR core reported in earlier research (e.g., Del Zanna 2012; Winebarger et al. 2012; Del Zanna & Mason 2018). The temperature and EM do, however, vary slightly over the course of the AR's evolution, which is consistent with the observed X-ray light curve. Following the arrival of AR 12749 and AR 12758, their activity decayed while rotating on the solar disk (Figure 1), which is why the temperature and EM decreased during their evolution, as indicated by the dashed vertical lines in Figure 5. After 2019 October 6, the EM for AR 12749 begins to rise as the AR weakens and the quiet-Sun emission takes precedence over the AR emission. Thus, after the AR has almost died and is very faint, the EM and temperature reach values close to the quiet-Sun temperature and EM. The temperature and EM for AR 12759 remain almost constant with time, as this AR crossed the solar disk without much decay in activity (Figure 1(c)).

5.2. Abundance Evolution

In contrast to the temperature and EM, the abundances of Mg, Al, and Si do not follow the X-ray light curve of any of the three ARs throughout their evolution (Figure 6). The abundances obtained for the low-FIP elements Al, Mg, and Si are consistently greater than the photospheric values,

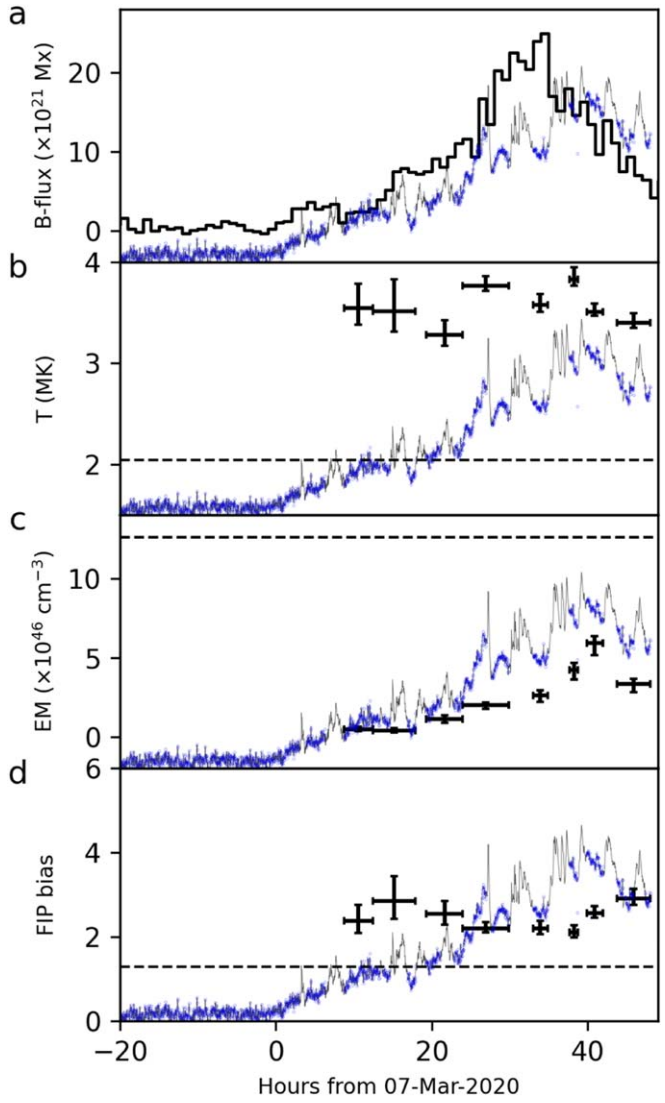

Figure 7. Results showing the emerging phase of AR 12758. The black curve in panel (a) shows the evolution of the total unsigned photospheric magnetic flux. Panels (b) and (c) show the evolution of temperature and EM. Panel (d) shows the evolution of the FIP bias for Si. The dashed lines in panels (b)–(d) represent the corresponding parameter for the background solar emission from the rest of the solar disk except the AR. The background gray curves in each panel represent the X-ray light curve observed by XSM, whereas the blue curves represent the selected times excluding the flaring period, representing the quiescent AR.

demonstrating a persistent FIP bias during the course of the AR. Note that the abundances are measured with respect to the continuum emission, which depends on the abundances of other elements, primarily oxygen.

After the emergence of AR 12758, the FIP bias was found to be almost constant throughout its decay phase. Similarly, during the decay of AR 12749, the FIP bias remains nearly constant, in contrast to certain earlier studies, such as Ko et al. (2016). They suggested a decreasing FIP bias in high-temperature plasma of more than 2 million degrees during the decay phase of an AR. The more established AR, AR 12759, which evolved without decaying much during its transit across the solar disk, also shows an almost constant FIP bias, similar to the other two ARs.

We do not find any relationship between the age of the AR and the FIP bias, as suggested in some previous papers, e.g., Del Zanna & Mason (2014) and Doschek & Warren (2019). Taking the oxygen abundance as 8.8 dex, the measured abundances for Mg and Si are within the range of coronal abundances reported in the literature (e.g., Feldman 1992; Fludra & Schmelz 1999; orange shaded regions in Figure 6). However, the Al abundance is ∼30%–60% higher. We note that the Al lines in the XSM spectra are blended with Mg lines. From Markov Chain Monte Carlo (MCMC) analysis (discussed in Appendix A), we find that there is no anticorrelation between the Mg and Al abundances. This suggests that the observed spectra do indeed require higher abundances of Al and cannot be explained by an enhancement of Mg abundances.

5.3. First Ionization Potential Bias during the Emergence of the Active Region Core

Though we do not find any relationship between the age of the AR cores and their FIP biases (Section 5.2), which remain constant, it is interesting to study the timescale on which the FIP bias developed during the emergence of the AR core. Such a study has been made possible using the finer (less than a day) time-resolved spectroscopy during the emerging phase (2020 March 7 to 2020 March 9) of AR 12758. During this period, we estimated the total unsigned photospheric magnetic flux as measured by HMI/SDO and shown in Figure 7(a) (black). The peak in the magnetic flux represents the time when the AR completely emerged onto the solar disk.

After the emergence, the unsigned magnetic flux is found to (temporarily) decrease. Figures 7(b) and (c) show the evolution of the AR core temperature and EM. With the emergence of the AR, the temperature becomes close to the AR core temperature of ∼3 MK, and the EM increases as the emitting plasma volume increases until it has emerged completely. We also derived the evolution of the FIP bias during this period, shown in Figure 7(d) for Si. During this period, as the emission from the Mg and Al line complex was weak compared with the background solar emission, the derived FIP bias for Mg and Al has a large uncertainty and is not shown here. Within ∼10 hr of the AR emergence, the FIP bias was already close to 2.5 and remained almost constant throughout the evolution. So the emerging hot core loops for this AR do not show any variation in the FIP bias, in agreement with previous suggestions. Recall that the variations in FIP bias reported earlier (e.g., Widing & Feldman 2001) were observed in the cool loops, not the hot core loops.

5.4. Enhanced Bias for Al

Figure 8 (red points) shows the average values of the FIP bias (relative to the photospheric abundance; Asplund et al. 2009) for all of the elements as a function of their FIP values. The lower-FIP element, Al (FIP = 5.99), is found to have the highest FIP bias of 5–6, whereas the low-FIP elements, Mg (FIP = 7.65) and Si (FIP = 8.15), are found to have a lower FIP bias of 2–2.5. The mid/high-FIP element, S, is found to have a much lower FIP bias close to unity. A higher FIP bias for Al is noteworthy and may point to an intriguing physical process. However, this may also be a modeling artifact.

One of the possibilities could be due to missing flux caused by the presence of multithermal plasma providing strong signals from emission lines of Al or Mg formed at different temperatures. To verify this, we have simulated the emission lines in the energy range of the Mg/Al line complex by

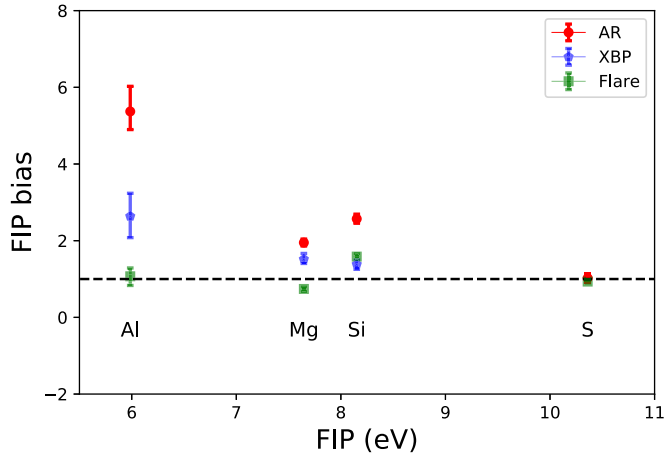

Figure 8. Variation of the FIP bias with the FIP of the elements. The red points are the averaged FIP bias for one of the ARs (AR 12749) reported in the present study. The blue points are the FIP bias for the XBPs as reported by Vadawale et al. (2021b). The green points are the measured FIP bias during the solar flare peak as reported by Mondal et al. (2021).

considering both the isothermal model and a multithermal model using the AR DEM of AR 12759, reported by Del Zanna et al. (2022; see Figure B1 in Appendix B). Similar line intensities from various ionization stages of Al and Mg can be seen in both the isothermal and multithermal models, confirming that the absence of the flux is not the result of multithermal plasma.

Another possibility is that the missing flux is caused by missing lines of Al or Mg (mostly satellite lines) that are not yet present in CHIANTI version 10. We have analyzed the high-resolution spectroscopic observations described by Walker et al. (1974) and found several observed lines that are missing in the database. However, the total missing flux, compared to the predicted flux by CHIANTI, is not enough to explain the anomalous Al abundance. However, the Walker et al. (1974) observations were taken during a high level of solar activity, so it is possible that the missing lines have a stronger contribution at 3 MK. The Al abundance is currently clearly overestimated by some degree.

Although this analysis is not conclusive enough to rule out Al's high FIP bias as an artifact, it is also not sufficient to conclude that it is not real. A higher Al FIP bias could be real. This might be explained by examining a few particular scenarios from the ponderomotive force model (Laming 2015) proposed by Laming (private communication), which could be investigated in a subsequent study.

The FIP bias of the quiet Sun (Vadawale et al. 2021b) and during flares (Mondal et al. 2021) was studied earlier using XSM. For visual inspection, a combined plot is generated (Figure 8). The blue points depict the FIP bias during the quiet period of the Sun when the disk emission is dominated by XBPs (Vadawale et al. 2021b). On the other hand, the green points represent the FIP bias during the peak of the solar flares, as reported by Mondal et al. (2021). In our present study, the FIP bias of an AR core (red points) shows a consistently higher value for all elements such as Al, Mg, and Si compared to that of the XBPs (green points). Since ARs possess a much higher magnetic field compared to XBPs, the ponderomotive force may play a crucial role (Laming 2015) in deciding the high value of the FIP bias in ARs. However, due to chromospheric evaporation, the FIP bias becomes near unity during flares. It is worth mentioning here that the abundance of oxygen (8.89 dex) considered in all of the abovementioned earlier works was the value prescribed by Fludra & Schmelz (1999). Even though in our present study, we consider a very similar value (8.8 dex), for confirmation's sake, we have also verified that the present results remain unchanged even if we change our oxygen abundance value to the value of Fludra & Schmelz (1999).

6. Summary

We present the evolution of plasma characteristics for three ARs using disk-integrated soft X-ray spectroscopic observations from XSM to make simultaneous line and continuum measurements. Carrying out a comprehensive study of an AR using the Sun-as-a-star mode observation is challenging because of the presence of multiple activities throughout the solar cycle. Unique XSM observations made during the minimum of solar cycle 24 allowed the study of the evolution of temperature, EM, and the abundances of Mg, Al, and Si for the individual ARs in the absence of any other noteworthy activity on the solar disk. Since the ARs were the principal contributors of disk-integrated X-rays during their evolution, the temperature and EM followed their X-ray light curve. The average temperature of all of the ARs is ~3 MK, close to the well-known temperature of the AR core. Irrespective of the activity and age of the ARs, the abundances or FIP biases of Al, Mg, and Si were found to be consistently greater than their photospheric values, without much variation. The abundance values develop within ~10 hr of the appearance of the AR during its emerging phase. Throughout the AR evolution, the low-FIP elements, Mg and Si, have an FIP bias of 2–2.5, whereas the mid-FIP element, S, has an average FIP bias of almost unity. The lowest-FIP element, Al, has a greater FIP bias of ~5–6. After discussing various modeling artifacts, the Al abundance appears to be overestimated, although the exact factor is unknown. The increased Al abundance could be real, implying that the low-FIP elements' degree of FIP bias is linked to their FIP values. Future spectroscopic studies to measure the FIP bias for more low-FIP elements (for example, Ca, whose FIP bias is between Al and Mg) would help us to better understand this phenomenon. In this regard, recent and upcoming X-ray spectrometers—for example, DAXSS (Schwab et al. 2020) on board INSPIRESat-1, SoLEXS (Sankarasubramanian et al. 2011) on board the upcoming Aditya-L1 observatory, the CubeSat Imaging X-ray Solar Spectrometer (Caspi et al 2021), and the rocket-borne spectrometer MaGIXS (Champey et al. 2022)—will be useful.

Finally, we stress that the abundances of Mg, Al, Si, and S are obtained from the line-to-continuum measurement in the 1.3–3 keV energy range, where the continuum is determined by the abundance of other elements, primarily oxygen. We assumed an average oxygen abundance obtained for the SW, and we have justified this choice. However, as the SW measurements indicate a significant O variability, our results have some uncertainty in terms of the absolute values (with respect to H) of abundance and FIP bias. In the future, for better measurement of the abundance close to the absolute scale, a simultaneous measurement of the oxygen abundance is needed.

Acknowledgments

We acknowledge the use of data from the Solar X-ray Monitor (XSM) on board the Chandrayaan-2 mission of the

Indian Space Research Organisation (ISRO), archived at the Indian Space Science Data Centre (ISSDC). The XSM was developed by the engineering team of the Physical Research Laboratory (PRL) led by Dr. M. Shanmugam, with support from various ISRO centers. We thank various facilities and the technical teams from all contributing institutes and Chandrayaan-2 project, mission operations, and ground segment teams for their support. Research at PRL is supported by the Department of Space, Govt. of India. We acknowledge the support from the Royal Society through international exchanges grant No. IES\R2\170199. G.D.Z. and H.E.M. acknowledge support from STFC (UK) via the consolidated grant to the atomic astrophysics group at DAMTP, University of Cambridge (ST\T000481\1). A.B. was the J C Bose National Fellow during the period of this work. We thank Dr. Martin Laming for the useful discussion on anomalous Al abundance. We are thankful to an anonymous referee for providing us with very useful feedback.

Facilities: Chandrayaan-2(XSM), SDO(AIA, HMI), Hinode(XRT).

Appendix A
Results of Markov Chain Monte Carlo Analysis

We carried out an MCMC analysis of the spectra to obtain the regions of parameter space that best fit the observed spectra. This was done using the "chain" method available within XSPEC. Figure A1 shows the corner plot of the results for the spectrum on 2019 October 1. The results show that all parameters are well constrained by the spectra. In particular, we note that there is no anticorrelation observed between the Al and Mg abundances, showing that the enhanced Al abundances obtained cannot be adjusted by enhancements in Mg abundances. Similar trends are observed for spectra of other days as well.

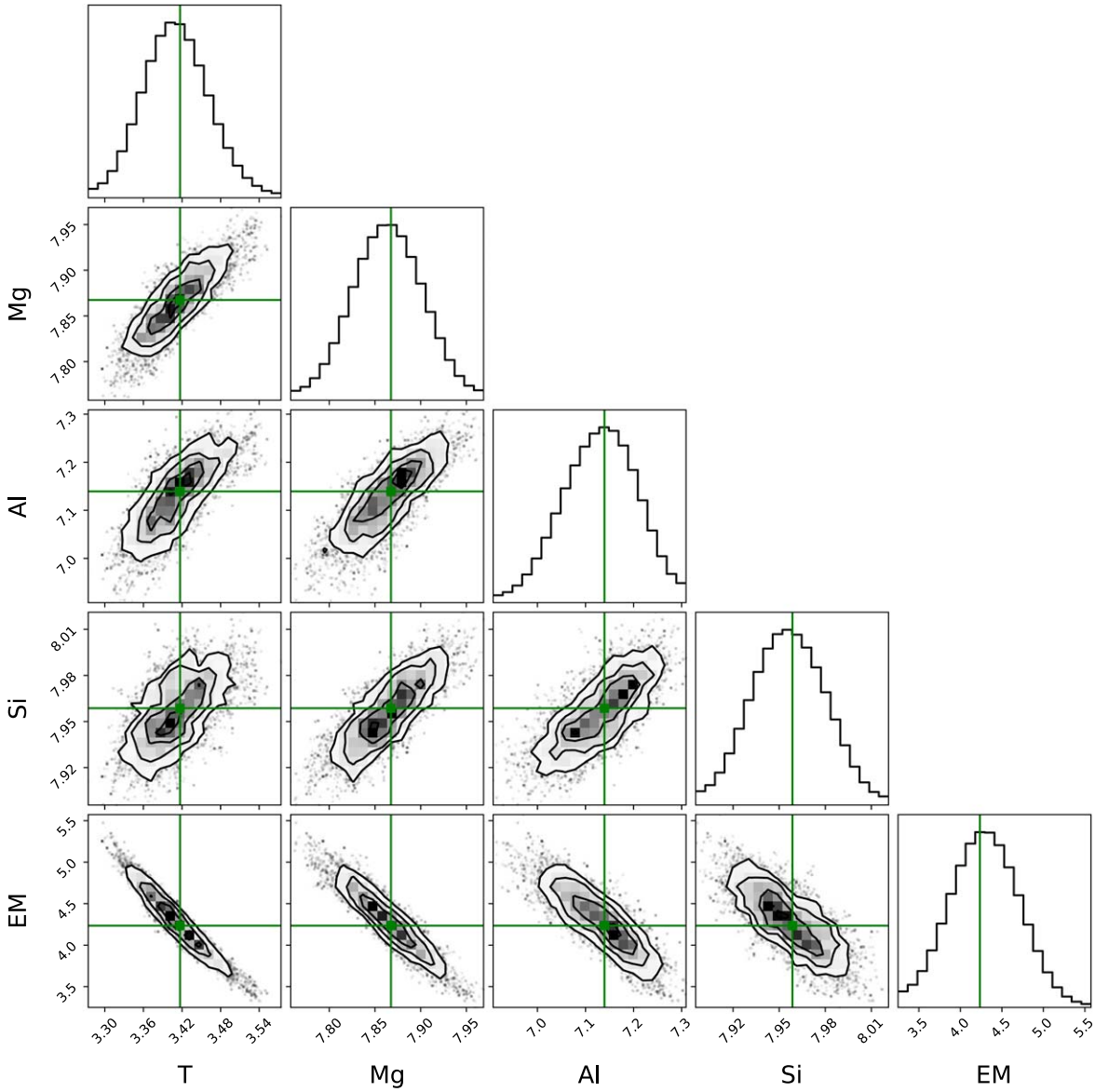

Figure A1. Corner plot depicting the results of the MCMC analysis for the fitted spectrum on 2019 October 1. The histograms depict the marginalized distribution associated with each parameter. The scatter plots are overlaid with contours representing 1σ, 2σ, and 3σ levels to show the correlations between all parameters. The best-fit parameters are represented by green lines.

Appendix B
Simulated Spectrum

To check the effect of temperature on the Mg/Al line fluxes in the XSM energy range of 1.55–1.70 keV, we have compared the simulated spectra in the same energy range by considering the isothermal and multithermal DEM models. Figure B1 shows the simulated 3 MK spectrum (blue) overplotted with the multithermal spectrum (red). The isothermal spectrum is generated for an EM of 10^{27} cm^{-5}. The multithermal spectrum is derived by using the reported quiescent AR DEM by Del Zanna et al. (2022), which was obtained from the Hinode/EIS observation of AR 12759. For the comparison of both spectra, we have normalized them with the corresponding line flux of Mg XI and Al XI–XII. Similar line intensities predicted by both isothermal and multithermal models indicate that spectra are insensitive to temperature in this case.

Appendix C
Dependence of Continuum on the Abundant Elements

We have measured the abundances of Mg, Al, Si, and S with respect to 1–3 keV continuum emission produced by three physical processes: thermal bremsstrahlung, free–bound, and two-photon. Among these three processes at an AR temperature of around 3 MK, the contribution of two-photon is almost negligible (<2%), whereas the free–bound emission contributes more than 80% (see Figure C1(b)). Thus, our measured abundances of Mg, Al, Si, and S will depend on the abundances of all other elements (except Mg, Al, Si, and S) that contribute to the free–bound and free–free emission. Hydrogen primarily determines the free–free continuum; however, the other heavy elements contribute to the free–bound emission. Among all of the elements, O and Ne are the primary contributors (nearly 80%) to the free–bound continuum (see Figure C1(b)).

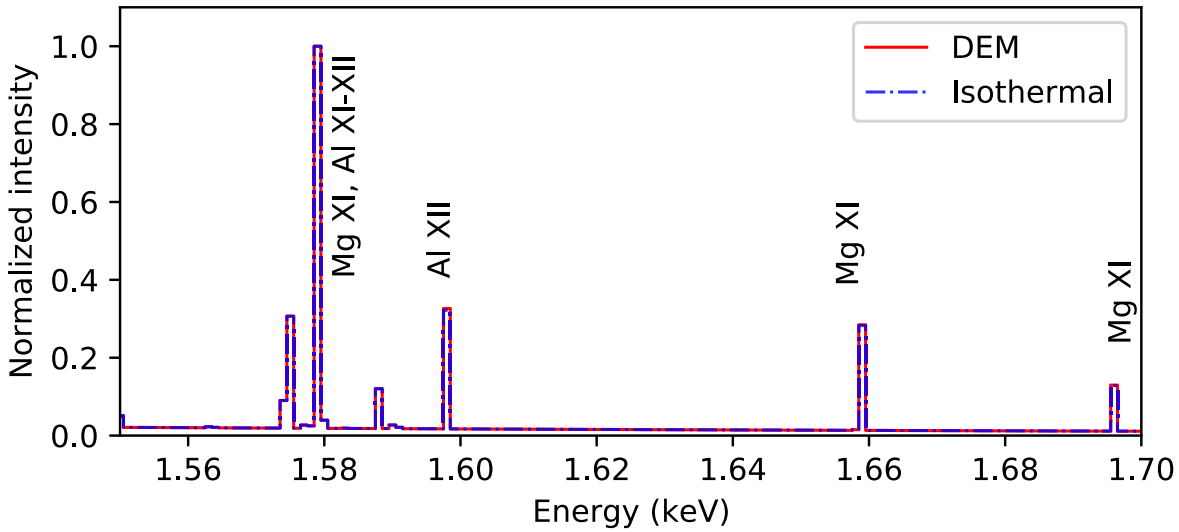

Figure B1. Simulated spectra from CHIANTI v 10 in the energy range of the Mg/Al line complex of the XSM observed spectrum. The red curve shows the multithermal spectrum, and the blue curve shows the isothermal spectrum.

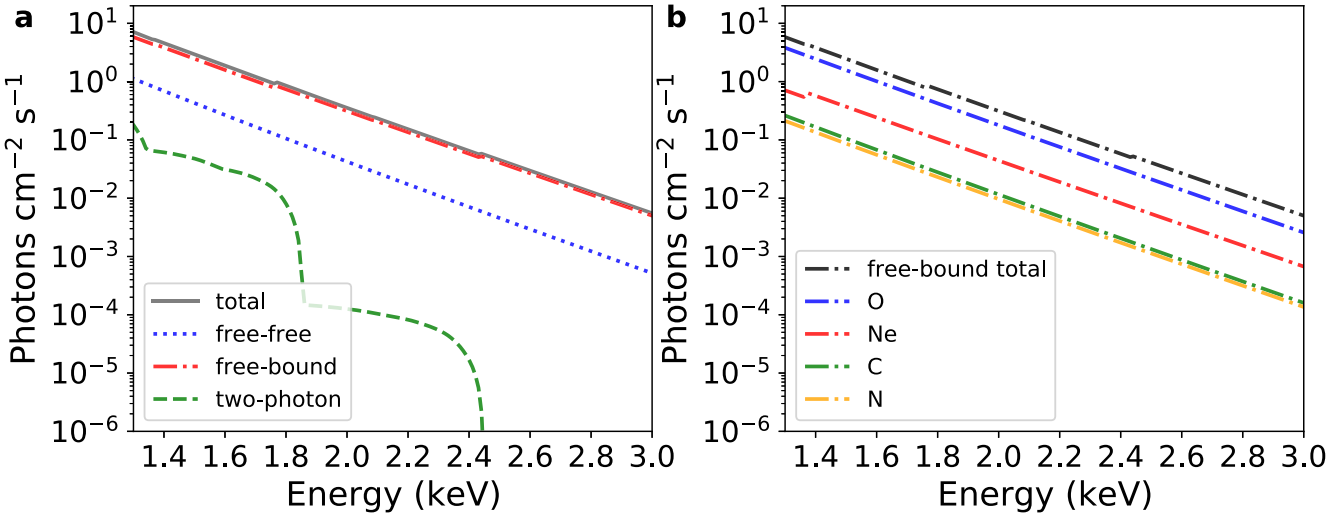

Figure C1. (a) Different components of the continuum spectrum in the energy range of 1–3 keV at 3 MK. (b) Contribution of different elements to the free–bound continuum. The total free–bound continuum is shown in black.

ORCID iDs

Biswajit Mondal https://orcid.org/0000-0002-7020-2826
Santosh V. Vadawale https://orcid.org/0000-0002-2050-0913
Giulio Del Zanna https://orcid.org/0000-0002-4125-0204
N. P. S. Mithun https://orcid.org/0000-0003-3431-6110
Aveek Sarkar https://orcid.org/0000-0002-4781-5798
Helen E. Mason https://orcid.org/0000-0002-6418-7914
P. Janardhan https://orcid.org/0000-0003-2504-2576
Anil Bhardwaj https://orcid.org/0000-0003-1693-453X

References

Arnaud, K., Dorman, B., & Gordon, C. 1999 XSPEC: An X-ray Spectral Fitting Package, Astrophysics Source Code Library, ascl:9910.005
Asplund, M., Amarsi, A. M., & Grevesse, N. 2021, A&A, 653, A141
Asplund, M., Grevesse, N., Sauval, A. J., & Scott, P. 2009, ARA&A, 47, 481
Baker, D., Brooks, D. H., Démoulin, P., et al. 2013, ApJ, 778, 69
Baker, D., Brooks, D. H., Démoulin, P., et al. 2015, ApJ, 802, 104
Baker, D., Brooks, D. H., van Driel-Gesztelyi, L., et al. 2018, ApJ, 856, 71
Bame, S. J., Asbridge, J. R., Feldman, W. C., Montgomery, M. D., & Kearney, P. D. 1975, SoPh, 43, 463
Bochsler, P. 2007, A&ARv, 14, 1
Brooks, D. H., Baker, D., van Driel-Gesztelyi, L., & Warren, H. P. 2017, NatCo, 8, 183
Brooks, D. H., Ugarte-Urra, I., & Warren, H. P. 2015, NatCo, 6, 5947
Brooks, D. H., & Warren, H. P. 2011, ApJL, 727, L13
Caspi, A., Shih, A. Y., Panchapakesan, S., et al. 2021, AAS Meeting, 238, 216.09
Champey, P. R., Winebarger, A. R., Kobayashi, K., et al. 2022, JAI, 11, 2250010
Dahlburg, R. B., Laming, J. M., Taylor, B. D., & Obenschain, K. 2016, ApJ, 831, 160
Del Zanna, G. 2003, A&A, 406, L5
Del Zanna, G. 2012, A&A, 537, A38
Del Zanna, G. 2013, A&A, 558, A73
Del Zanna, G. 2019, A&A, 624, A36
Del Zanna, G., & Mason, H. E. 2003, A&A, 406, 1089
Del Zanna, G., & Mason, H. E. 2014, A&A, 565, A14
Del Zanna, G., & Mason, H. E. 2018, LRSP, 15, 5
Del Zanna, G., Mondal, B., Rao, Y. K., et al. 2022, ApJ, 934, 159
Doschek, G. A., & Warren, H. P. 2019, ApJ, 884, 158
Dwivedi, B. N., Curdt, W., & Wilhelm, K. 1999, ApJ, 517, 516
Feldman, U. 1992, PhyS, 46, 202
Feldman, U., Schuhle, U., Widing, K. G., & Laming, J. M. 1998, ApJ, 505, 999
Feldman, U., & Widing, K. G. 2002, PhPl, 9, 629
Fludra, A., & Schmelz, J. T. 1999, A&A, 348, 286
Freeland, S. L., & Handy, B. N. 1998, SoPh, 182, 497
Gloeckler, G., & Geiss, J. 1989, in AIP Conf. Ser. 183, Cosmic Abundances of Matter, ed. C. J. Waddington (Melville, NY: AIP), 49
Ko, Y.-K., Young, P. R., Muglach, K., Warren, H. P., & Ugarte-Urra, I. 2016, ApJ, 826, 126
Laming, J. M. 2004, ApJ, 614, 1063
Laming, J. M. 2009, ApJ, 695, 954
Laming, J. M. 2012, ApJ, 744, 115
Laming, J. M. 2015, LRSP, 12, 2
Laming, J. M. 2017, ApJ, 844, 153
Mihailescu, T., Baker, D., Green, L. M., et al. 2022, ApJ, 933, 245
Mithun, N., Vadawale, S., Patel, A., et al. 2021, A&C, 34, 100449
Mithun, N. P. S., Vadawale, S. V., Sarkar, A., et al. 2020, SoPh, 295, 139
Mithun, N. P. S., Vadawale, S. V., Zanna, G. D., et al. 2022, ApJ, 939, 112
Mondal, B., Klimchuk, J. A., Vadawale, S. V., et al. 2023, ApJ, 945, 37
Mondal, B., Sarkar, A., Vadawale, S. V., et al. 2021, ApJ, 920, 4
Nama, L., Mondal, B., Narendranath, S., & Paul, K. T. 2023, SoPh, 298, 55
Pottasch, S. R. 1963, ApJ, 137, 945
Saba, J. L. R., & Strong, K. T. 1993, AdSpR, 13, 391
Sankarasubramanian, K., Ramadevi, M. C., Bug, M., et al. 2011, AsInC, 2, 63
Schwab, B. D., Sewell, R. H. A., Woods, T. N., et al. 2020, ApJ, 904, 20
Shanmugam, M., Vadawale, S. V., Patel, A. R., et al. 2020, CSci, 118, 45
Sheeley, N. R. J. 1995, ApJ, 440, 884
Sheeley, N. R. J. 1996, ApJ, 469, 423
Testa, P., Martinez-Sykora, J., & De Pontieu, B. 2023, ApJ, in press
Vadawale, S., Shanmugam, M., Acharya, Y., et al. 2014, AdSpR, 54, 2021
Vadawale, S. V., Mithun, N. P. S., Mondal, B., et al. 2021a, ApJL, 912, L13
Vadawale, S. V., Mondal, B., Mithun, N. P. S., et al. 2021b, ApJL, 912, L12
Von Steiger, R., Zurbuchen, T., & McComas, D. 2010, GeoRL, 37, L22101
Walker, A. B. C. J., Rugge, H. R., & Weiss, K. 1974, ApJ, 188, 423
Widing, K. G. 1997, ApJ, 480, 400
Widing, K. G., & Feldman, U. 1993, ApJ, 416, 392
Widing, K. G., & Feldman, U. 2001, ApJ, 555, 426
Winebarger, A. R., Warren, H. P., Schmelz, J. T., et al. 2012, ApJL, 746, L17
Young, P. R., & Mason, H. E. 1997, SoPh, 175, 523